Guidewire detection and 3D-Reconstruction for image-guided surgery

Anirudh Choudhary (achoudhary46@gatech.edu)
Special Problem Project Report

***Abstract*— The treatment of peripheral arterial disease is typically performed using catheters and requires surgeon to manually navigate the guidewire to the affected region within the artery. Different image modalities such as CT, X-Ray can be employed by the surgeon to navigate the guidewire to the target location. Delays during navigation can lead to increased radiation exposure to the clinician, particularly if the X-Ray images are acquired using a X-Ray machine such as C-Arm. Thus, automated guidewire navigation using images acquired with a C-Arm is critical. Accurate continuous 3D tracking of guidewire tip is important during automated navigation and comprises of three key tasks: subject pose estimation, guidewire segmentation and reconstruction, and path planning. The guidewire tracking needs to be fast and should be able to achieve high sub-mm accuracy. In this project, we propose fully-automated approaches to address each sub-task and evaluate their performance using sample guidewire X-Ray images. Our approach is able to robustly segment guidewire under various occlusions and perform 3D reconstruction with acceptable accuracy. We also compare two path-planning strategies and develop an efficient pose estimation algorithm.**

I. INTRODUCTION

Peripheral Arterial Disease (PAD) is a common cardiovascular disease associated with the accumulation of plaque in the peripheral blood vessels, which restricts blood flow in the affected region. Reduced blood flow leads to decreased oxygenation of the concerned tissue which leads to tissue death and subsequently, life threatening scenario [1]. Catheter-based procedures have been quite popular for treating patients with PAD [2], primarily due to their minimally-invasive nature compared to open-heart surgery as well as reduced trauma for the patients due to localized intervention. During the procedure, a catheter containing a guidewire is inserted through a vasculature and the cardiologist uses real-time imaging system to visualize the relevant anatomy and navigate the guidewire, till it reaches the blocked blood vessel. Guidewires are frequently used for many cardiovascular procedures and various studies have been proposed to improve their tracking during surgery. Detection and segmentation of wire-like structures is a challenging problem for medical imaging applications as well as computer vision. Since X-Rays are harmful, these devices have been designed to employ small X-Rays doses. As a result, the shot noise leading to a signal-to-noise ratio proportional to the square root of the number of photons received by each X-Ray detector unit, the acquired signal exhibits a low signal-to-noise ratio. Here, our main interest is the segmentation and accurate position estimation of the guidewire from X-Ray images acquired using a C-Arm. Despite the high spatial resolution ($\approx$ 0.5 mm per pixel) of C-Arm images, detection of guidewires is challenging due to the following reasons:

1) Low thickness of guidewire ($\approx$ 2-3 pixels)
2) Significant non-rigid motion of the guidewire between subsequent frames, both due to guidewire translation and C-Armś rotation
3) 2D projections of 3D anatomy leads to overlapping structures (primarily vessel edges) leading to occlusion as well as presence of non-relevant thin and curvilinear structures similar to guidewire, which interfere with segmentation.

Automated 3D reconstruction of guidewire needs to be accurate for wire-tip tracking as well as robust to noise and imaging artifacts. During reconstruction, multiple images are acquired by moving the C-Arm along the plane parallel to the curvature plane of the guidewire. This leads to repeated radiation exposure for personnel involved and hence, the complete process of guidewire segmentation and re-construction needs to be real-time. Moreover, initial path generation for guidewire navigation is important, not only to understand the feasibility of the procedure, but also to ensure a safer procedure by continuously performing motion planning to correct guidewire misalignment and avoid interaction with the vessel boundaries. Given these challenges, in this project, we evaluate multiple approaches for three key tasks critical for automated navigation and analyse their performance:

1) Guidewire segmentation: We propose a novel two-step approach which extracts the guidewire and is also robust to the motion of the C-Arm.
2) 3D-Reconstruction: We compare filtered back projection and iterative approaches for accurate guide reconstruction.
3) Initial Path Planning: We compare two path-planning approaches for initial path generation for navigating guidewire within the 3D phantom.

Additionally, since during the surgical procedure, the patient can be aligned in an arbitrary pose, we need to perform an initial 3D pose estimation and subsequently correct for the angular displacement during 3D reconstruction. We evaluate a framework for 2D/3D image registration between C-Arm X-Ray images and 3D CT scan, comparing keypoint and pixel similarity-based approaches. We leverage digitally reconstructed radiographs (DRR) with GPU acceleration for generating 2D projections of the CT volume and register them against the C-Arm images.

A. Related Work

1) Guidewire Segmentation: Conventional guidewire segmentation methods, relying on image features such as pixel intensity, texture or histogram, fail to detect guidewires

accurately. Methods based on active contours or level sets are prone to image artifacts and other wire-like objects. Brost et al. [3] developed a model-based lasso catheter tracking algorithm. However, their method required manual initialization or a model provided by the detection method and did not generalize to guidewires. While multiple approaches for catheter segmentation have been proposed, they primarily rely on catheter electrodes or magnetic markers and are not relevant to guidewire segmentation, due to lack of relevant features. Approaches for guidewire segmentation can be classified into three groups: a) tracing methods; b) shortest path methods and c) bottom-up grouping method. Bottom-up growing methods rely on detecting line segments initially and building the guidewire curve from the segments using segment linking and curvature-based optimization criterion. Honnorat et al. [4] present a bottom-up approach relying on steerable filters and tensor voting to identify relevant line segments (primitives) which is followed by clustering and ordering-based linking. Most approaches enhance the wire-like structures such as guidewire using Hessian-based filter by computing the vesselness or rely on curvilinear structures detector for extracting the support of the guidewire. Beyar et al. [5] used a combination of filter-based method and Hough transform to extract wire-like objects and fit a polynomial curve onto them. Hessian filtering is combined with a B-spline fitting-based approach using the gradient image derived from Hessian filter and the catheter shape from the previous frame. The drawback with these approaches is the manual initialization required in the first frame of fluoroscopic sequence and the requirement that the length of catheter should not change much between frames. Machine learning-based approaches which leverage probabilistic approach or recently deep learning segmentation frameworks such as U-Net have been leveraged to counter these challenges. Navab et al. [6] used randomly generated deformable models while Barbu et al. [7] used marginal space learning to track the target object using manual annotations. Wang et al. [8] applied region proposal network (RPN) on X-Ray images achieving close to 90% segmentation accuracy. Ambrosini et al. [9] proposed a fully-automatic U-Net based segmentation approach, wherein the catheter is segmented using the CNN and centerline is extracted using skeletonization and branch linking.

2) 3D Guidewire Reconstruction: Guidewire reconstruction is typically done using biplanar images and primarily two types of approaches have been proposed: backprojection-based and epipolar-constraint-based. Baert et al. [10] proposed the first approach to multiview 3D reconstruction of curvilinear objects, which required generating a 2D curve for each image by placing interest points. Papalarozou et al. [11] proposed another approach for rigid and deformable objects. Limited studies focus on 3D guidewire position reconstruction using monoplanar images. Buckner et al. [12] proposed a recursive probability density propagation based approach to build a 3D probability distribution of the wire position and used particle filter to perform temporal update of the distribution. Walsum et al. [13] leverage minimum cost algorithm to select appropriate solution, however, the uncertainty in reconstruction is not fully addressed due to the complex self-intersecting shapes generated from the guidewire in projections. Esthappan et al. [14] use a 2D/3D registration to find a rigid body transform to align the predetermined 3D model of guidewire tip to single 2D image. Petkovic et al. [15] leveraged prior knowledge of the blood vessels in 3D volume to constrain a backprojection-based approach using monoplanar images acquired from C-Arm. Most of the approaches rely on preexisting 3D volume to constrain the solution space. To alleviate these limitations, Hoffman et al. [3] presented a semiautomatic approach requiring detection using manual clicks followed by point correspondence and triangulation to achieve final reconstruction. Baur et. al. [**?**] proposed a robust approach for catheters in fluoroscopic sequences by relying on epipolar gemoetry-based triangulation and incorporating prior knowledge about the catheters in a probabilistic graphical model, subsequently minimizing the reprojection and epipolar projection errors.

3) Path Planning: Given a 3D vascular model, path planning involves computing trajectories which are used to define the ideal position and direction of guidewire during navigation. Path planning algorithms thus aim to solve a two-point boundary value problem in R^3 in the presence of obstacles. A semiautomatic method of trajectory planning for vascular navigation was proposed in [16] which used a level-set segmentation to find nodes corresponding to the vessel's center. Cheng et al. [17] applied skeletonization techniques to extract blood vessel centerlines to perform efficient path planning for endovascular surgical tools. Traditional studies relied on simplified techniques such as vessel centerline extraction or deterministic path planning while recent approaches explore collision-free approaches used for robot-path planning with Rapidly Exploring Random-Trees (RRT) [18] being quite popular. RRT is a popular graph-based method which is suited for problems involving obstacles and differential constraints. RRT constructs a space-filling tree by randomly sampling points and expanding into largest Voronoi regions of the graph. Reachability-based constraints [19] have been applied on RRTs to make them efficient by restricting their search space towards nodes closer to the goal. Schafer et al. [20] proposed a graph-representation-based technique to compute guidewire paths inside the carotid artery which returns a unique solution for specific vessel geometries. Fauser et al. [21] proposed a cubic-Bezier spline based RRT to compute curvature constrained trajectories. Recent research has leveraged robotics studies and explored the application of the 'learning from demonstration' framework by training machine learning models on clinician's demonstrations. Chi et al. [22] proposed a robotic platform for semiautonomous catheter movement that leverages anatomical landmarks and non-rigid registration to map catheter tip trajectories in different anatomical settings. The catheter proximal and tip motion patterns were jointly encoded using a Gaussian Mixture Model trained on demonstrations and the model was used as a trajectory generator for different subjects.

We follow the following outline in this report. In Section II, we introduce the components of our imaging system and describe the approaches explored for guidewire segmentation, path planning, 3D reconstruction and initial pose estimation. We present our experimental setup in Section III and present the results in Section IV highlighting the efficacy of our proposed approaches.

II. MATERIALS AND METHODS

A. Imaging System

In this paper, we use the OEC 9800 Plus system (GE Healthcare, Chicago, USA) to acquire images. The field of view is approximately 20 cm and the system has a resolution of $512\,\text{px} \times 512\,\text{px}$. We retrieved the live images from the system using the Orion HD (Matrox, Dorval, Canada) frame grabber in combination with MIL-Lite and the Matlab® Image Acquisition Toolbox™ (MathWorks, Natick, USA). We leveraged the distortion correction approach presented in [23] for all experiments.

B. Mechanical Setup

Vessel Phantom and Guidewire: We use a 3D printed coronary vessel phantom for this project. The phantom comprises of the heart and two major vessels surrounding the heart which bifurcate into thinner branches.The guidewire is machined from superelastic Nitinol tubes (Johnson Matthey®, London, United Kingdom) and has an outer diameter 0.889 mm (0.035" or 2.67 F).

C. Guidewire Segmentation

We follow a two-step approach for segmenting the guidewire and localizing its tip. The first steps involves highlighting the vessel boundaries and generating an initial mask for separating guidewire pixels from vessel boundary pixels. We apply distortion and isocentre correction on original X-Ray images before applying our segmentation algorithm. Given the corrected X-Ray image I, we apply 'Difference of Gaussian' based filter to highlight the vessel-like structures, using smoothened (I_s) and original versions of the image I. Smoothing is done using median filtering (filter size = 9px x 9px) leading to removal of guidewire from I_s, which helps us in delineating the vessel boundaries only. We leverage the B-COSFIRE filter [24] which has been shown to be effective in localizing vessel-like structures. Before filtering, we apply anisotropic diffusion-based filtering to remove noise and enhance boundary regions in I. We also apply adaptive histogram equalization, to account for fluctuating X-Ray intensities between subsequent frames, and enhance the contrast of acquired X-Ray image. We apply thresholding on COSFIRE filter outputs of smoothened and original images to obtain masks (I_{sC} and I_C) corresponding to vessel boundaries and vessel boundaries + guidewire regions. We subtract I_{sC} from I_C and apply morphological operations along with region area-based selection to obtain a binary mask I_{mg} corresponding to the regions pertaining to guidewire.

In the second step, we focus on segmenting the region around the tip of the guidewire. We follow the popular curvilinear structure detection approach proposed by Steger *et* al. [25] to highlight ridge structures in the contrast enhanced image. We use the parameter values of $sigma = 1$, $t_{lower} = 1$ and $t_{higher} = 3$ for applying the ridge detector. Ridge detection segments the guidewire very well but also responds to vessel related edges. Hence, to separate the guidewire related pixels, we leverage the binary mask I_{mg} and identify the ridges belonging to the guidewire.

We compared alternate filtering approaches for determining vesselness, which rely on computing the eigenvalues of the Hessian matrix. These included Meijering neuriteness, Sato tubeness, Frangi vesselness and Hessian vesselness filters. We also explored using keypoint-correspondence based matching using SIFT to track guidewire across multiple images but found it to be suboptimal particularly when the images were acquired at angles more than 20° apart.

D. Path Planning

To enable safe and accurate navigation of the guidewire within the vessel, initial path planning is vital, as it enables us to visualize the ideal path to be followed by the guidewire and define a set of target points to be followed while moving inside the vessel. We formulate path-planning as a shortest path problem between the start and end points defined by the user. Since our initial navigation problem is relatively simple i.e. the start and goal points in the phantom are easily reachable without major obstacles or curvature, we follow a deterministic approach which relies on using a predefined cost function. The shortest path problem is transformed to defining a cost function for various paths within the vessel structure. Consider a curve P, which defines a navigation path from point S to any point, x. In general, the curve P is a minimal path with respect to a metric γ if it minimizes the following energy functional:

$$E_\gamma(P) = \int_P \gamma(P(l), \dot{P}(l))dl \tag{1}$$

where l is the arclength. The solution to the minimum path integral can be obtained by defining a minimal distance map, $D : c \rightarrow R^+$ defined as $D(x) = \min_P E(P)$ for any path P linking S to x in the domain $c \subset R^2$. We leverage the 2D Fast Marching Method (FMM) proposed by Sethian *et al.* [26] to extract the shortest path P. Given an image I, FMM satisfies the Eikonal equation:

$$||\nabla D(x)|| = \gamma(x), \forall x \in I; \quad D(S) = 0 \tag{2}$$

wherein D may be regarded as the arrival time of a front propagating from S with velocity $1/\gamma(x)$. The map D has only one local minimum at starting point S and the key goal of FMM is to define an efficient $\gamma(x)$ to propagate the front efficiently. FMM has been successfully applied for minimal-path extraction and centerline computation in robotic and surgical navigation studies [27] [28].

1) 2D Shortest Path Computation: We initially formulate our path-planning algorithm on a simple 2D phantom. To constrain the shortest path within the vessel region, we

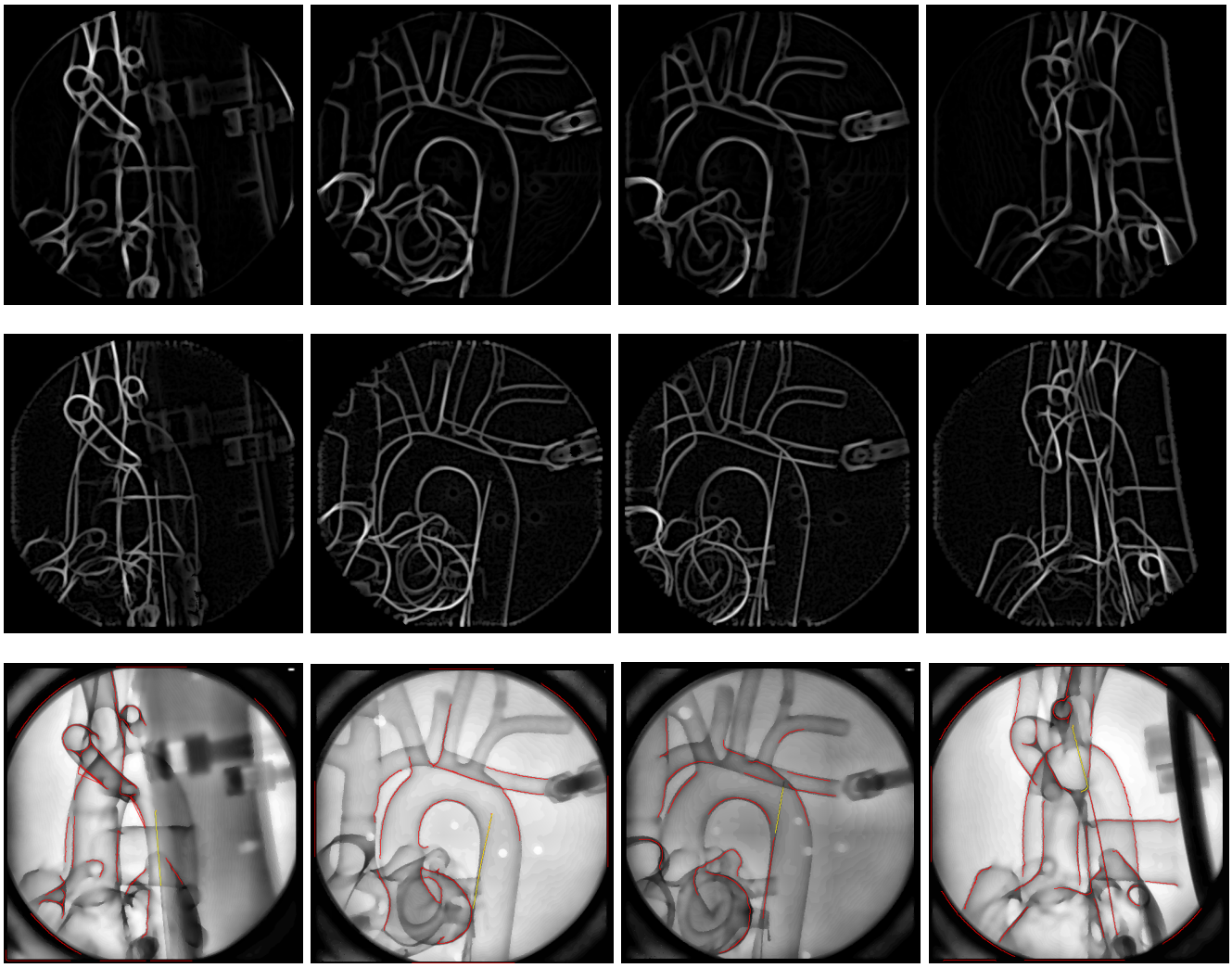

Fig. 1: Guidewire Segmentation: Row 1 - COSFIRE filter output with guidewire being removed (through smoothing), Row 2- COSFIRE filter output with guidewire and vessel boundaries captured, Row 3 - Guidewire tip segment localization via ridge detection; segmented tip section highlighted in 'Yellow'

segment the vessel's internal region and define a binary mask I_v upon which FMM is applied. To construct I_v, we rely on edge-based segmentation rather than intensity-based thresholding due to intensity variations within the phantom. We smooth the image using a median filter (span=9) and apply adaptive histogram equalization to enhance the contrast. Post preprocessing, we apply Hessian-based multi-scale Frangi vesselness filter [29] to detect the ridges corresponding to phantom's walls and threshold the filtered image using Otsu thresholding to obtain a binary mask I_w. After inverting I_w and analyzing the various connected components based on their area and bounding box dimensions, the vessel's internal region is delineated and the smooth mask I_v is defined. Before applying FMM on the extracted mask, we shrink it by 10 pixels so that the shortest-path maintains minimal distance from phantom's wall. To define target points on P, we fit a third-order spline and sub-sampled 6% points. Fig. 5 highlights the distance map and extracted paths along with target points.

2) 3D Centerline Extraction: After successfully exploring the Fast Marching-based approach in 2D settings, we focus on applying FMM to the 3D vascular model obtained from the CT scan. We compare FMM with another popular approach relying on graph-based centerline extraction using the software VMTK [30]. Whereas FMM relies on shortest path and would typically prefer straight path with minimal curves, centerlines follow a maximum-obstacle avoidance approach following the curvature of the 3D volume. Centerlines were extracted using active contour level set segmentation and performing a weighted geodesic search over Voronoi diagram. Voronoi diagram is a partition of a plane with n points into convex polygons, such that each polygon contains exactly one generating point and every point in a given polygon is closest to its generating point. Voronoi diagrams are created using Delaunuy Traingulation [31]. Centerlines are computed as the paths defined on the Voronoi diagram that minimize the integral of the radius of maximal inscribed spheres along the path. This is equivalent to finding the shortest paths in the radius metric using a formulation similar to FMM, by

Fig. 2: Failure of alternate vesselness filters to delineate the guidewire and vessel boundaries completely; Sato, Meijering, Frangi and Hessian (left to right)

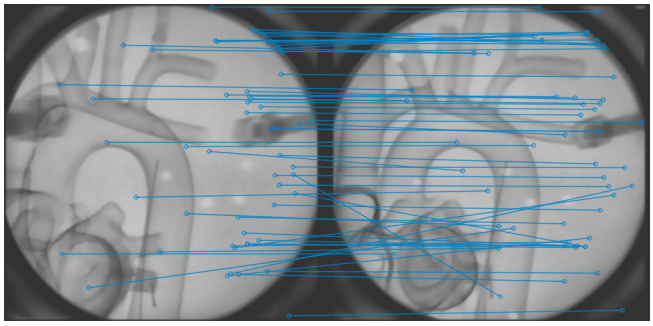

Fig. 3: Failure of SIFT-based keypoint matching in estimating translation between two frames at 60° and 80°; Very few keypoints are detected on the phantom

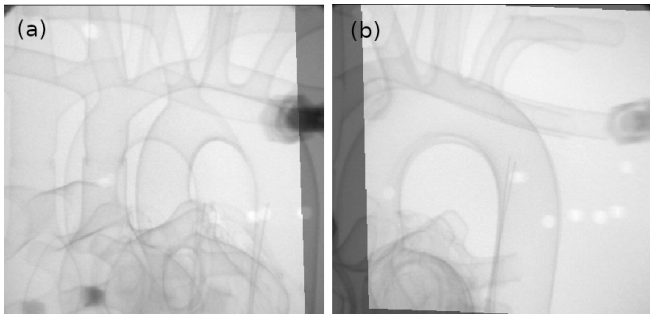

Fig. 4: Rigid registration-based tracking: (a) Failure to register between frames at 20° and 40°; (b) Successful registration between frames at 60° and 80°

propagating a wave from a source point and using inverse of the radius as the wave speed. The arrival times of the wave for all the points on Voronoi diagram is computed and gradient of arrival times is used to construct the path from the target point. For every point belonging to the Voronoi diagram, there's a sphere centered in that point that

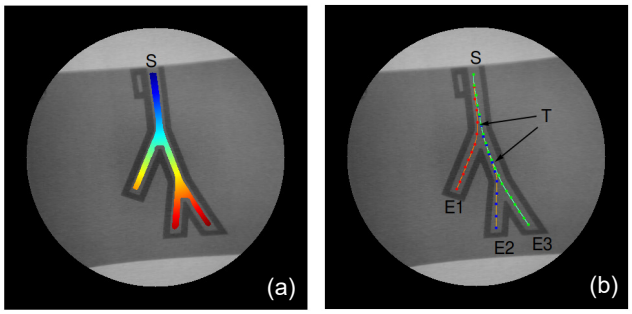

Fig. 5: Illustration of path planning for guidewire navigation: a) Distance-map generated using 2D Fast Marching Method with starting point, S, and b) 3 shortest paths starting from S ($S \rightarrow E1$, $S \rightarrow E2$, $S \rightarrow E3$) with target points, T.

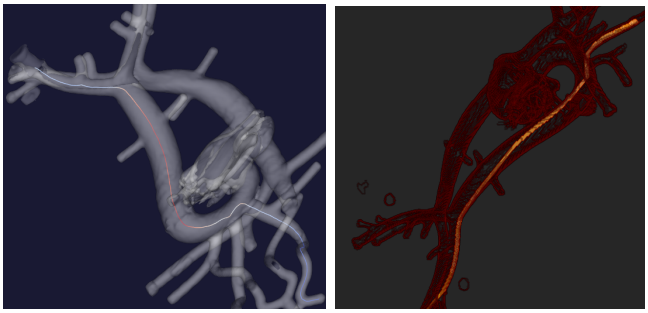

Fig. 6: Illustration of initial paths computed for 3D-CT vascular: a) Centerline extraction using Voronoi diagram b) Shortest path computed using 3D FMM

is a maximal inscribed sphere. Each point on the centerline is thus associated with a corresponding maximal inscribed sphere radius.

Given a 3D volume V, we perform hole filling and surface smoothing before extracting the centerline. This leads to V_b which is our binary volume for constraining the path search. Pre-processing is important since centerlines are influenced by the surface geometry of the ROI. The output of VMTK is a set of centerline points, $C \in R^3$ which naturally constrain the guidewire position by vessel geometry. We also apply 3D FMM algorithm between the same set of start and end points and compare the shortest path with longer curved path computed using centerlines. The 3D FMM is conceptually similar to 2D FMM described earlier.

E. 3D-Reconstruction[1]

Accurate reconstruction of guidewire using monoplanar image is an ill-constrained problem, given the multiple poses of guidewire which could lead to same projection image. As such typically two or more C-Arm images are utilized to determine the guidewire pixels in reconstructed 3D volume. Since multiple X-Ray images require frequent repoisitioning of C-Arm which is time-consuming, the reconstruction of guidewire in a particular configuration needs to be performed with minimal number of images. Here, we compare Filtered Back Projection and iterative reconstruction-based approaches along with evaluating splines for smoothing

[1]Work done jointly with Florian Heemeyer

the guidewire. For each method, we compare its accuracy with varying 2D input image counts and C-Armś angular displacements.

1) Filtered Back Projection (FBP): Backprojection is a standard method of reconstructing CT images. Backprojection simply runs the projections back through the image to obtain a rough approximation of the original volume. These projections interact constructively in the regions corresponding to the actual object in 3D volume. A problem with backprojection is the blurring artifacts that occur in other parts of the reconstructed image. Hence, FBP [32] leverages a high pass filter(typically a ramp filter in noiseless cases) to eliminate blurring. We use FBP as our baseline. An example of the C-Arm imaging geometry is shown in Fig. 7. The C-Arm imaging configuration is defined by the world position of the X-Ray source and the world position and the number and dimensions of pixels of the image plane(detector). The perspective geometry needs to be known and the projection matrix computation requires relative distances of source from imaging volume and detector. These values are derived from the C-Arm manual. We perform distortion correction and isocentric alignment of X-Ray images before applying FBP.

2) Iterative Reconstruction: We leverage gradient-based iterative construction algorithm called FISTA [33] with Total Variation based regularization. The objective function for FISTA is given as:

$$min_x||P(x)-I||^2+2\lambda||x||_{TV} \tag{3}$$

where I is the observed 2D image data, $P(x)$ is a linear projection mapping applied on a volume x and λ is the regularization coefficient.

3) Spline Smoothing: We initially use an interpolation-based smoothing wherein only significant deviations in 3D wire are removed. Spline-based approaches [15] have been leveraged to smoothen the 3D reconstructed curve and we explore fitting natural cubic splines to generate smooth guidewire curves.

F. Initial Patient Pose Estimation

1) DRR Generation: DRR generation addresses the problem of finding X-Ray detector response using the Beer-Lambert law [34]. DRR generation approaches have been grouped into analytic(ray-tracing) and statistical(Monte Carlo(MC) Simulation) approaches. Ray-tracing tries to model the attenuation of photon as it passes through the anatomical region, the total attenuation along various 3D lines is computed and applied to photons traveling in that particular direction [35]. While most ray tracing approaches consider only single type of material and fails to account for beam hardening. Moreover, given its a analytic approach, statistical processes such as scattering during the image formation cannot be modeled. MC methods evaluate the probability of photon-matter interaction and its sequence determines the attenuation [36]. It requires material decomposition in CT volume which is typically achieved using thresholds called Houndfield units (HU) and spectra of the emitter. MC is very realistic and but is computationally very expensive. This leads to various simulation challenges related to realistic nature of modeling as well as fast generation of images.In our case, we leverage DeepDRR [37], which was proposed to overcome these challenges and leverages segmentation of typical materials in CT(air, soft tissue and bone) to determine individual contribution of each material to the total attenuation density. Each material's contribution to the total attenuation density at detector position u are computed using a given geometry (defined by projection matrix $P \in R^{3x4}$) and X-Ray spectral density $p_0(E)$ via ray-

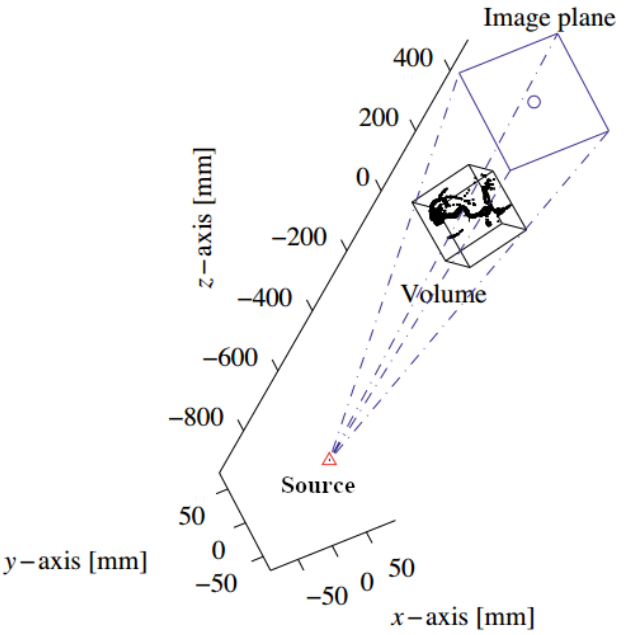

Fig. 7: C-Arm Imaging Configuration (Petkovic et al. [15])

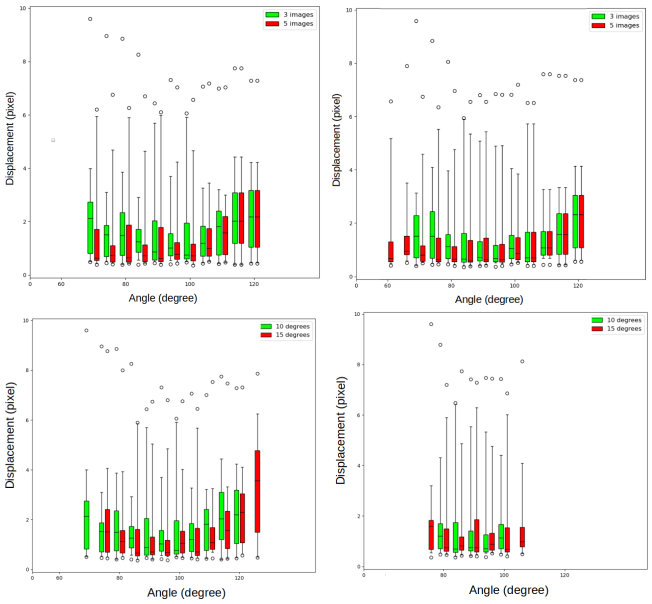

Fig. 8: Reconstruction Accuracy: Evaluating filtered back projection based reconstruction for varying image count and angular displacement between images: a)3 vs 5 images b)10 vs 15 degrees

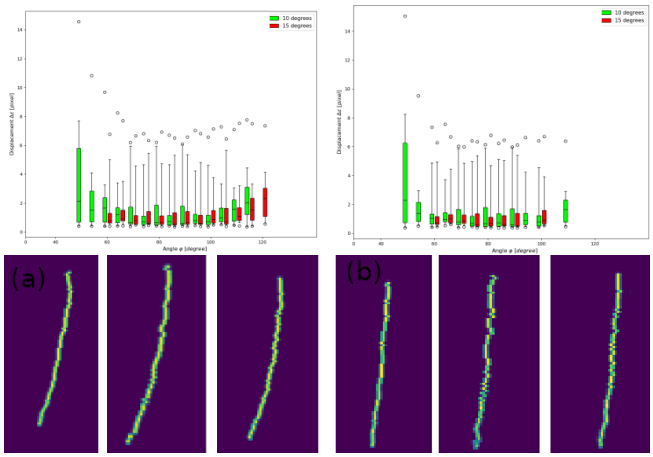

Fig. 9: Row 1 - Reconstruction Accuracy of FBP and TV-regularized FISTA; Row 2: 2D projections of 3D reconstruction for FBP with spline smoothing, FBP with interpolated smoothing and FISTA with regularization (in order) a)Forward projections at 65° b)Forward projections at 45°

tracing:

$$p(u) = \int p(E,u)du \quad (4)$$

$$= \int p_0(E)exp(\sum_{m\in M} \delta(m,M(x))(\frac{\mu}{\rho})_m(E) \int \rho(x)dl_u)dE \quad (5)$$

where $\delta(.,.)$ is Kronecker delta, l_u is 3D ray connecting the source position and 3D location of detector pixel u determined by P, $(\frac{\mu}{\rho})_m(E)$ is the material and energy dependent attenuation coefficient and $\rho(x)$ is the material density derived at position x based on HU values.

Also, since we are using the ASTRA toolbox which allows us to compute forward projection, we compared the DRRs derived from ASTRA with DRRs generated using DeepDRR.

2) 2D Registration: We select two reference X-Ray images at 0° and 90° of our 3D phantom in horizontal position (ideal setting). To determine the subject pose, we perform a spatial alignment between the DRR and reference images using rigid image registration. We follow an iterative approach, starting with DRRs generated at 5° and matching them with reference image to find the best aligned DRR. This gives us a rough initial pose estimate which we refine iteratively by comparing DRRs within ±5°, generated at an angular displacement of 1°. The second step gives a finer estimate of actual pose. We use the Euler Transform to perform the registration and use Mean Squared Difference(MSD) and Normalized Mutual Information(NMI) based similarity measures to determine the best aligning DRRs. We leverage the *elastix* [38] toolbox to perform the registration, which gives us multiple options for image transformations, metrics and points sampling. The cost function for registration to be minimized is given by:

$$C(T_w;I_F,I_M) = -S(T_w,I_F,I_M) + \gamma P(T_w) \quad (6)$$

where S is the similarity measure mentioned above, γ is the regularization coefficient, P is the penalty term, I_F is the fixed image, I_M is the moving image and T_w is the image-to-image transformation parameterized by w.

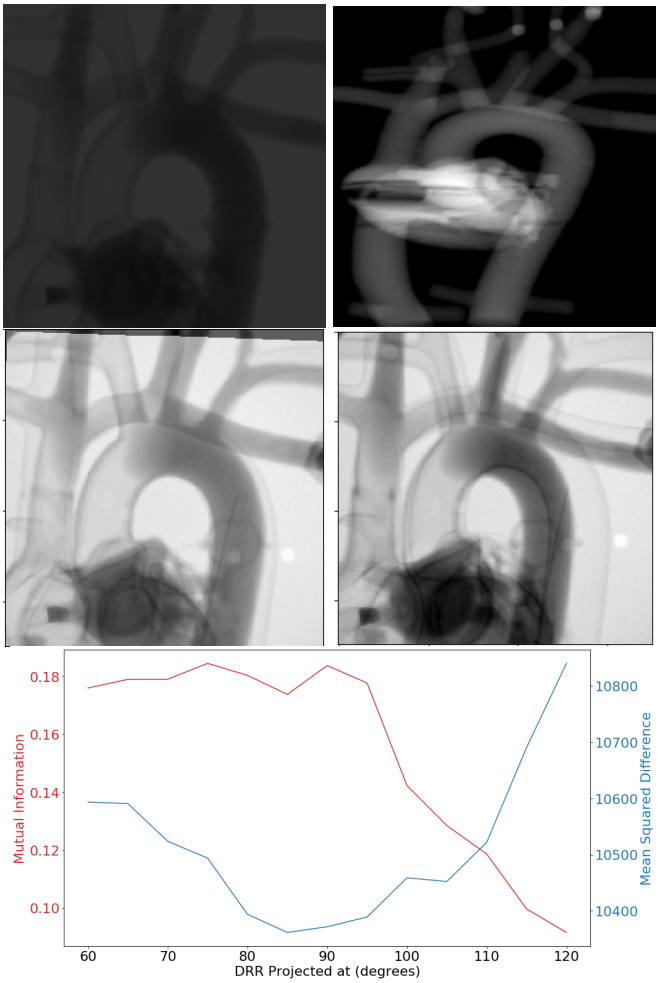

Fig. 10: Initial Pose Estimation: Row 1 - DRR Projections obtained from DeepDRR and ASTRA toolbox; Row 2 - Registration of DRR with X-Ray reference image a)DRR at 90°, b)DRR at 75°. Row 3 - Similarity metrics computed between DRR projections at multiple angles and reference X-Ray image at 90; NMI values are high and quite close at both 75° and 90° while MSD values are quite apart °

III. EXPERIMENTAL SETUP

1) Guidewire Segmentation: We acquired ≈ 240 X-Ray images at 5° orbital shift with 4 different positions of the guidewire in the vascular phantom. This enables us to evaluate our algorithm for multiple guidewire and C-Arm configurations.

2) 3D Reconstruction: 10 images of the guidewire in standard configuration (predetermined curvature) were utilized to evaluate FBP and FISTA reconstruction methods. The images were acquired at angles $\theta_i \in [40°, 130°]$ at an interval of 10°. The guidewire was segmented manually in the acquired images to define the ground-truth 2D images I_{gI} for evaluation. To find the reconstruction error, the 2D projections I_{ri} of reconstructed guidewire were obtained at θ_i and pair of nearest guidewire-located points were

determined from I_r and I_g. Subsequently, euclidean norm was computed between the 2D position in I_g and corresponding 2D position in I_r. This was calculated for all 10 angles. The reconstruction error, referred to as pixel displacement is given by: $\delta_{\alpha_k} = ||\hat{p}_{rk} - p_{gk}||^2$

3) Path Planning: We created a 3D vascular dicom dataset by segmenting the phantom from the CT-scan using thresholding and used it to create paths.

4) Pose Estimation: We use the 3D vascular dataset to generate DRRs for angles ranging from 0° to 130° at an interval of 5° and evaluate the similarity metric at each angle post registering the DRR with X-Ray image acquired at 90° orbital position of C-Arm. Our ground truth pose is zero degrees and DRR projection at 90° should maximally align with the X-Ray image.

IV. RESULTS AND FUTURE WORK

1) Guidewire Segmentation: : We were able to segment guidewire accurately and localize the guidewire segment starting from the tip across multiple C-Arm positions (Fig 1) using combination of a vessel highlighting filter and simple ridge detector. We found B-COSFIRE filter to outperform other vesselness filters in capturing vessel boundaries anf guidewire. We tried tracking vessel areas and region surrounding guidewire betwween frames, using SIFT and rigid registration, but found both approaches to be unreliable, particularly in C-Arm orbital position below 40°. Additionally, we also explored deep learning-based object tracking frameworks such as SiamMask but found them prone to failure. While our segmentation performs wuite well, we need to integrate it with a tracking method to robustly segment the guidewire. The next step is to improve the robustness of ridge detector and leverage Multiple Hypothesis Tracking [39] to track the ridges corresponding to the guidewire. Additionally, we could also explore b-splines to model the guidewire and deform it using the gradient field computed using COSFIRE filters, this approach however assumes limited distortion and motion of the guidewire and might be prone to failure.

2) Path Planning: : We present the results of centerline-based and shortest-path (using 3D FMM) planning in Fig. 6. The centerline path follows the curvature of the vessels and maintains maximal distance from vessel boundaries. Shortest-path computes relatively straight paths and maintains minimal distance from vessel boundary. This might be helpful in guidewire navigation due to the mechanical constraints of the guidewire and easier motion control under straight paths. However, maintaining a minimal distance from vessel boundaries is critical and hence, we can explore rapidly-exploring random trees which are robust to obstacles and can be constrained using splines and goal reachability to generate smoother paths, particularly in regions with larger curvature.

3) 3D Reconstruction: : All reconstruction approaches are able to achieve median displacement error within 2 pixels($\approx 0.9mm$). We also found that imaging around a plane within $pm30$ degrees of the true curvature plane leads to reconstruction with no significant increase in displacement error. This is critical since the C-Arm has a limited orbital span and moreover, images acquired between 35-50 ° are corrupted due to interference from the operating table. Hence, for curvature planes not lying within ideal angular positions of the C-Arm, the reconstruction has to be performed from nearest ideal angular position. We found a combination of 5 images with 15° angular separation to result in lowest displacement error in forward projections with respect to true guidewire position Fig 8. We also found spline-based smoothing and TV-regularization to result in smoother reconstruction compared to interpolation-based smoothing (Fig 9). FISTA-based iterative approach led to lower displacement errors compared to FBP, however the average reconstruction time was almost 10 times(20 sec) of FBP(2 sec).

4) Initial Pose Estimation: We found DRR derived using DeepDRR to be much better than ray-tracing algorithm provided by ASTRA (Fig 10). DeepDRR also takes into account different anatomical materials for X-Ray attenuation and simulates scattering and beam hardening in an improved manner. We had to apply contrast-enhancement on generated DRRs to enhance their quality for subsequent registration. To determine the true subject pose using image-registration between DRR and X-Ray image, we found image similarity metrics to perform quite well in responding maximally to actual patient pose. For future work, we suggest combining image and edge-map based similarities to make the algorithm more robust. Moreover, a single metric such as NMI might respond similarly to two different positions (75° and 90°) in our case and we propose to use a combination of metrics such as NMI and MSD for robustness.

ACKNOWLEDGEMENT

Research reported in this report was supported by the National Heart, Lung, And Blood Institute of the National Institutes of Health under Award Number R01HL144714. The work was performed under the guidance of Professor Jaydev Desai with certain sections (distortion correction and guidewire reconstruction) done in collaboration with Florian Heemeyer. The author is grateful to Florian Heemeyer and Achraj Sarma for the imaging and mechanical setup. The content is solely the responsibility of the authors and does not necessarily represent the official views of the National Institutes of Health.

REFERENCES

[1] R. L. Muir, "Peripheral arterial disease: Pathophysiology, risk factors, diagnosis, treatment, and prevention," *Journal of Vascular Nursing*, vol. 27, pp. 26–30, June 2009.

[2] K. Ouriel, "Peripheral arterial disease," *The Lancet*, vol. 358, pp. 1257–1264, Oct. 2001.

[3] M. Hoffmann, A. Brost, C. Jakob, F. Bourier, M. Koch, K. Kurzidim, J. Hornegger, and N. Strobel, "Semi-automatic catheter reconstruction from two views," in *International Conference on Medical Image Computing and Computer-Assisted Intervention*, pp. 584–591, Springer, 2012.

[4] N. Honnorat, R. Vaillant, and N. Paragios, "Discrete methods for guide-wire segmentation and tracking," 2011.

[5] D. Palti-Wasserman, A. M. Brukstein, and R. P. Beyar, "Identifying and tracking a guide wire in the coronary arteries during angioplasty from x-ray images," *IEEE Transactions on Biomedical Engineering*, vol. 44, no. 2, pp. 152–164, 1997.

[6] O. Pauly, H. Heibel, and N. Navab, "A machine learning approach for deformable guide-wire tracking in fluoroscopic sequences," in *International Conference on Medical Image Computing and Computer-Assisted Intervention*, pp. 343–350, Springer, 2010.

[7] A. Barbu, V. Athitsos, B. Georgescu, S. Boehm, P. Durlak, and D. Comaniciu, "Hierarchical learning of curves application to guidewire localization in fluoroscopy," in *2007 IEEE Conference on Computer Vision and Pattern Recognition*, pp. 1–8, IEEE, 2007.

[8] L. Wang, X.-L. Xie, G.-B. Bian, Z.-G. Hou, X.-R. Cheng, and P. Prasong, "Guide-wire detection using region proposal network for x-ray image-guided navigation," in *2017 International Joint Conference on Neural Networks (IJCNN)*, pp. 3169–3175, IEEE, 2017.

[9] P. Ambrosini, D. Ruijters, W. J. Niessen, A. Moelker, and T. van Walsum, "Fully automatic and real-time catheter segmentation in x-ray fluoroscopy," in *International Conference on Medical Image Computing and Computer-Assisted Intervention*, pp. 577–585, Springer, 2017.

[10] S. A. Baert, M. A. Viergever, and W. J. Niessen, "Guide-wire tracking during endovascular interventions," *IEEE Transactions on Medical Imaging*, vol. 22, no. 8, pp. 965–972, 2003.

[11] C. Papalazarou, P. M. Rongen, and P. H. de With, "Surgical needle reconstruction using small-angle multi-view x-ray," in *2010 IEEE International Conference on Image Processing*, pp. 4193–4196, IEEE, 2010.

[12] M. Brückner, F. Deinzer, and J. Denzler, "Temporal estimation of the 3d guide-wire position using 2d x-ray images," in *International Conference on Medical Image Computing and Computer-Assisted Intervention*, pp. 386–393, Springer, 2009.

[13] T. Van Walsum, S. A. Baert, and W. J. Niessen, "Guide wire reconstruction and visualization in 3dra using monoplane fluoroscopic imaging," *IEEE transactions on medical imaging*, vol. 24, no. 5, pp. 612–623, 2005.

[14] J. Esthappan, M. A. Kupinski, L. Lan, and K. Hoffmann, "A method for the determination of the 3d orientations and positions of catheters from single-plane x-ray images," in *Proceedings of the 22nd Annual International Conference of the IEEE Engineering in Medicine and Biology Society (Cat. No. 00CH37143)*, vol. 3, pp. 2029–2032, IEEE, 2000.

[15] T. Petković, R. Homan, and S. Lončarić, "Real-time 3d position reconstruction of guidewire for monoplane x-ray," *Computerized medical imaging and graphics*, vol. 38, no. 3, pp. 211–223, 2014.

[16] C. Wang, R. Moreno, and Ö. Smedby, "Vessel segmentation using implicit model-guided level sets," in *MICCAI Workshop" 3D Cardiovascular Imaging: a MICCAI segmentation Challenge", Nice France, 1st of October 2012.*, 2012.

[17] I. Cheng, A. Firouzmanesh, A. Lelevé, R. Shen, R. Moreau, V. Brizzi, M.-T. Pham, T. Redarce, P. Lermusiaux, and A. Basu, "Enhanced segmentation and skeletonization for endovascular surgical planning," in *Medical Imaging 2012: Image-Guided Procedures, Robotic Interventions, and Modeling*, vol. 8316, p. 83162W, International Society for Optics and Photonics, 2012.

[18] S. M. LaValle, "Rapidly-exploring random trees: A new tool for path planning," 1998.

[19] A. Shkolnik, M. Walter, and R. Tedrake, "Reachability-guided sampling for planning under differential constraints," in *2009 IEEE International Conference on Robotics and Automation*, pp. 2859–2865, IEEE, 2009.

[20] S. Schafer, V. Singh, K. R. Hoffmann, P. B. Noël, and J. Xu, "Planning image-guided endovascular interventions: guidewire simulation using shortest path algorithms," in *Medical Imaging 2007: Visualization and Image-Guided Procedures*, vol. 6509, p. 65092C, International Society for Optics and Photonics, 2007.

[21] J. Fauser, R. Chadda, Y. Goergen, M. Hessinger, P. Motzki, I. Stenin, J. Kristin, T. Klenzner, J. Schipper, S. Seelecke, *et al.*, "Planning for flexible surgical robots via bézier spline translation," *IEEE Robotics and Automation Letters*, vol. 4, no. 4, pp. 3270–3277, 2019.

[22] W. Chi, J. Liu, H. Rafii-Tari, C. Riga, C. Bicknell, and G.-Z. Yang, "Learning-based endovascular navigation through the use of non-rigid registration for collaborative robotic catheterization," *International journal of computer assisted radiology and surgery*, vol. 13, no. 6, pp. 855–864, 2018.

[23] F. Heemeyer, A. Choudhary, and J. P. Desai, "Pose-aware c-arm calibration and distortion correction for guidewire tracking and image reconstruction," in *2020 International Symposium on Medical Robotics (ISMR)*, IEEE, Apr. 2020 (*accepted*).

[24] G. Azzopardi, N. Strisciuglio, M. Vento, and N. Petkov, "Trainable cosfire filters for vessel delineation with application to retinal images," *Medical image analysis*, vol. 19, no. 1, pp. 46–57, 2015.

[25] C. Steger, "An unbiased detector of curvilinear structures," *IEEE Transactions on pattern analysis and machine intelligence*, vol. 20, no. 2, pp. 113–125, 1998.

[26] J. A. Sethian, "A fast marching level set method for monotonically advancing fronts," *Proceedings of the National Academy of Sciences*, vol. 93, no. 4, pp. 1591–1595, 1996.

[27] M. Wei, Q. Wang, Y. Li, W.-M. Pang, L. Liang, J. Wang, K. K. L. Wong, D. Abbott, J. Qin, and J. Wu, "Centerline extraction of vasculature mesh," *IEEE access*, vol. 6, pp. 10257–10268, 2018.

[28] K. Belharet, D. Folio, and A. Ferreira, "Simulation and planning of a magnetically actuated microrobot navigating in the arteries," *IEEE Transactions on Biomedical engineering*, vol. 60, no. 4, pp. 994–1001, 2012.

[29] A. F. Frangi, W. J. Niessen, K. L. Vincken, and M. A. Viergever, "Multiscale vessel enhancement filtering," in *International conference on medical image computing and computer-assisted intervention*, pp. 130–137, Springer, 1998.

[30] L. Antiga and D. A. Steinman, "Vmtk: vascular modeling toolkit," *VMTK, San Francisco, CA, accessed Apr*, vol. 27, p. 2015, 2006.

[31] J. W. Brandt and V. R. Algazi, "Continuous skeleton computation by voronoi diagram," *CVGIP: Image understanding*, vol. 55, no. 3, pp. 329–338, 1992.

[32] H. Turbell, *Cone-beam reconstruction using filtered backprojection*. PhD thesis, Linköping University Electronic Press, 2001.

[33] A. Beck and M. Teboulle, "Fast gradient-based algorithms for constrained total variation image denoising and deblurring problems," *IEEE transactions on image processing*, vol. 18, no. 11, pp. 2419–2434, 2009.

[34] J. H. Hubbell and S. M. Seltzer, "Tables of x-ray mass attenuation coefficients and mass energy-absorption coefficients 1 kev to 20 mev for elements z= 1 to 92 and 48 additional substances of dosimetric interest," tech. rep., National Inst. of Standards and Technology-PL, Gaithersburg, MD (United . . . , 1995.

[35] D. B. Russakoff, T. Rohlfing, K. Mori, D. Rueckert, A. Ho, J. R. Adler, and C. R. Maurer, "Fast generation of digitally reconstructed radiographs using attenuation fields with application to 2d-3d image registration," *IEEE transactions on medical imaging*, vol. 24, no. 11, pp. 1441–1454, 2005.

[36] A. Badal and A. Badano, "Accelerating monte carlo simulations of photon transport in a voxelized geometry using a massively parallel graphics processing unit," *Medical physics*, vol. 36, no. 11, pp. 4878–4880, 2009.

[37] M. Unberath, J.-N. Zaech, S. C. Lee, B. Bier, J. Fotouhi, M. Armand, and N. Navab, "Deepdrr–a catalyst for machine learning in fluoroscopy-guided procedures," in *International Conference on Medical Image Computing and Computer-Assisted Intervention*, pp. 98–106, Springer, 2018.

[38] S. Klein, M. Staring, K. Murphy, M. A. Viergever, and J. P. Pluim, "Elastix: a toolbox for intensity-based medical image registration," *IEEE transactions on medical imaging*, vol. 29, no. 1, pp. 196–205, 2009.

[39] C. Kim, F. Li, A. Ciptadi, and J. M. Rehg, "Multiple hypothesis tracking revisited," in *Proceedings of the IEEE International Conference on Computer Vision*, pp. 4696–4704, 2015.